Collective excitations and flat-band plasmon in twisted bilayer graphene near the magic angle

Xueheng Kuang, Zhen Zhan [ORCID],[*] and Shengjun Yuan[†]

Key Laboratory of Artificial Micro- and Nano-structures of Ministry of Education and School of Physics
and Technology, Wuhan University, Wuhan 430072, China

Twisted bilayer graphene with tiny rotation angles have drawn significant attention due to the observation of the unconventional superconducting and correlated insulating behaviors. In this paper, we employ a full tight-binding model to investigate collective excitations in twisted bilayer graphene near the magic angle. The polarization function is obtained from the tight-binding propagation method without diagonalization of the Hamiltonian matrix. With the atomic relaxation considered in the simulation, both damped and undamped plasmon modes are discovered near the magic angle under both room temperature and superconductivity transition temperature. In particular, an undamped plasmon mode in narrow bands can be directly probed in magic angle twisted bilayer graphene at superconductivity transition temperature. The undamped plasmon mode is tunable with angles and gradually fades away with both temperature and chemical potential. In practice, the flat bands in twisted bilayer graphene can be detected by exploring the collective plasmons from the measured energy loss function.

I. INTRODUCTION

Twisted bilayer graphene (TBG), where one sheet of graphene rotates relatively to the other, has recently attracted extensive interest in the scientific community. In TBG, one degree of freedom—the rotation angle—is introduced to tune its electronic properties. Experimental investigations are focusing on the properties of TBG with rotation angle $1.05°$—the so-called magic angle [1], where a plethora of fantastic phenomena, for instance, superconductivity [2,3], localized and correlated states [4–8], charge-ordered states [9], and quantum anomalous Hall effect [10], are constantly observed. Recently, plasmons arising from interband collective excitations have been detected by utilizing the scattering-type scanning near-field optical microscope(s-SNOM) at TBG with $1.35°$ [11]. Unique plasmons, such as flat and chiral plasmons, emerge in TBG [12–17]. Interestingly, flat plasmons detected in magic angle systems could be used to mediate the unconventional superconductivity [18,19] and give rise to the linear resistivity observed in the experiment [20]. Consequently, the importance of electron-electron interactions provokes us to gain insights into collective excitations in TBG, in particular, near the magic angle.

The full tight-binding (TB) model [21–26] and simplified continuum model [1,27–34] are widely used to investigate the electronic properties of TBG. Within the frame of these two models, the calculated properties of TBG can be in good agreement with experimental ones [5,11,35–37]. In general, if only low-energy properties are required, one could be prone to adopt simplified continuum models since the TBG near the magic angle contains over 10 000 atoms in its moiré

unit cell. In this case, it is difficult to obtain eigenvalues and corresponding eigenstates via the diagonalization of the huge Hamiltonian matrix in the TB model. For instance, optical conductivity and plasmonic properties of the TBG are studied by using the continuum model without considering the atomic relaxation [12,29,38]. As indicated in both experimental and theoretical works, relaxation has non-negligible effects to the electronic properties of the TBG, especially for relatively small twist angles [24,31,34,39]. Therefore, after taking into account the out-of-plane relaxation, the continuum model is subsequently used to analyze plasmons in doped and undoped TBG [11,13,40]. Nevertheless, continuum models used in TBG are simply effective near small twist angles or at low energies. It is not a universal method to investigate a wide range of angles and to consider the local electronic environment near each atom. Moreover, the atomic relaxation implemented in continuum models are derived from the TB results [23,25,31]. By using a tight-binding propagation method (TBPM) in the frame of a full TB model, very large structures with the number of atoms up to hundreds of millions can be studied [41]. The TBPM is based on the numerical solution of the time-dependent Schrödinger equation with additional averaging over random superposition of basis states. More importantly, the substrate effect, strain, physical defect, electric and magnetic fields can be easily implemented in our method [42–44] to study how they affect plasmonic properties. Last but not least, by combining the Kubo formula with TBPM, we could explore plasmonic properties in huge samples over a large energy range. Hence, as an atomic-scale approach, such a full TB model without diagonalization is still meaningful to study electronic and optical properties of TBG with a large range of twist angles [45].

In this paper, beyond those aforementioned continuum models, we systematically investigate the plasmonic properties of TBG near the magic angle by using the TBPM. We

---

[*]zhen.zhan@whu.edu.cn
[†]s.yuan@whu.edu.cn

modulate the interlayer interaction of the relaxed TBG with twist angle 1.35° to reproduce correctly the plasmons detected in a recent experiment [11]. Therefore, the Kubo formula implemented in the TBPM is accurate enough to investigate the relaxed TBG with tiny rotation angles. Then, plasmon spectra of TBG with rotation angles 1.35° and 1.05° for temperatures at both 300 K and 1 K are calculated. We observe that two collective plasmon modes are detected in TBG near the magic angle, that is, a damped mode at the high energy range and an undamped one in the low energy range. In the full TB model, the low-energy plasmons that are attributed to the collective excitations among the flat bands are sensitive to the temperature and doping effects. Such undamped plasmon is of keen interest for a bunch of applications, for instance, quantum information science and high-Q resonators.

This paper is organized as follows. In Sec. II, the TB model and computational methods are introduced, followed by the validity of the Kubo formula implemented in the TBPM. In Sec. III, the plasmon spectrums of TBG near the magic angle are illustrated at both 300 K and 1 K, and also with various chemical potentials. Finally, we give a summary and discussion of our work.

II. METHODS

A. Full tight-binding model

A parameterized full TB model with the commensurate approach to construct atomic structures of TBG has been used to successfully reproduce experimental findings [36,37]. In this paper, we also use the commensurate method to construct TBG with different rotation angles θ [37]. In the TB model, only p_z orbitals are taken into account; we construct the Hamiltonian of the TBG as

$$H = \sum_i \epsilon_i |i\rangle\langle i| + \sum_{\langle i,j \rangle} t_{ij} |i\rangle\langle j|, \tag{1}$$

where $|i\rangle$ is the p_z orbital located at $\mathbf{r}_i$, ϵ_i is the on-site energy of orbital i, which is set to -0.814 eV to ensure that the Fermi energy of TBG is at zero, and $\langle i, j \rangle$ is the sum over index i and j with $i \neq j$. According to the Slater-Koster (SK) formalism, the hopping integral t_{ij}, interaction between two p_z orbitals located at $\mathbf{r}_i$ and $\mathbf{r}_j$ has the form [46]

$$t_{ij} = n^2 V_{pp\sigma}(r_{ij}) + (1 - n^2) V_{pp\pi}(r_{ij}), \tag{2}$$

where $r_{ij} = |\mathbf{r}_j - \mathbf{r}_i|$ is the distance between i and j sites, with n as the direction cosine along the direction $\mathbf{e}_z$ perpendicular to the graphene layer. The SK parameters $V_{pp\pi}$ and $V_{pp\sigma}$ follow

$$V_{pp\pi}(r_{ij}) = -t_0 e^{q_\pi(1 - r_{ij}/d)} F_c(r_{ij}),$$
$$V_{pp\sigma}(r_{ij}) = t_1 e^{q_\sigma(1 - r_{ij}/h)} F_c(r_{ij}), \tag{3}$$

where $d = 1.42$ Å and $h = 3.349$ Å are the nearest in-plane and out-of-plane carbon-carbon distances, respectively, t_0 and t_1 are commonly reparameterized to fit different experimental results [25,26]. The parameters q_σ and q_π satisfy $\frac{q_\sigma}{h} = \frac{q_\pi}{d} = 2.218$ Å^{-1} and the smooth function is $F_c(r) = (1 + e^{(r-r_c)/l_c})^{-1}$, in which l_c and r_c are chosen as 0.265 and 5.0 Å, respectively.

B. Density of states

The density of states (DOS) for TBG is calculated by using the TBPM [41] in the frame of a full TB model. The TBPM makes it possible to obtain the electronic properties for large-scale quantum systems, for instance, the DOS of TBG with rotation angle θ down to 0.48°[37] and of a dodecagonal graphene quasicrystal [47,48],

$$D(E) = \frac{1}{2\pi N} \sum_{p=1}^{N} \int_{-\infty}^{\infty} e^{iEt} \langle \varphi_p(0)|e^{-iHt}|\varphi_p(0)\rangle dt, \tag{4}$$

where $|\varphi_p(0)\rangle$ is one initial state with the random superposition of basis states at all sites N. In all the calculations, the accuracy of the electronic properties can be guaranteed by utilizing a large enough system with more than ten million atoms. For instance, in all the calculations, the number of the atoms in the supercell is ten million. The number of time integration steps is 4096, which gives an energy resolution of 3.7 meV (15 eV/4096).

C. Dynamical polarization and dielectric function

Dynamical polarization can be obtained by combining the Kubo formula [49] with TBPM as [50]

$$\Pi_K(\mathbf{q}, \omega) = -\frac{2}{S} \int_0^{\infty} dt\, e^{i\omega t} \mathrm{Im} \langle \varphi | n_F(H) e^{iHt}$$
$$\times \rho(\mathbf{q}) e^{-iHt} [1 - n_F(H)] \rho(-\mathbf{q}) | \varphi \rangle, \tag{5}$$

where $n_F(H) = \frac{1}{e^{\beta(H-\mu)}+1}$ is the Fermi-Dirac distribution operator, $\beta = \frac{1}{k_B T}$ being T the temperature and k_B the Boltzmann constant, μ is the chemical potential, $\rho(\mathbf{q}) = \sum_i c_i^\dagger c_i \exp(i\mathbf{q} \cdot \mathbf{r}_i)$ is the density operator, and S is the area of the unit cell in TBG. The dynamical polarization function also can be obtained from the Lindhard function in a full TB model as [51]

$$\Pi(\mathbf{q}, \omega) = -\frac{g_s}{(2\pi)^2} \int_{BZ} d^2\mathbf{k} \sum_{l,l'} \frac{n_F(E_{\mathbf{k}l}) - n_F(E_{\mathbf{k}'l'})}{E_{\mathbf{k}l} - E_{\mathbf{k}'l'} + \hbar\omega + i\delta}$$
$$\times |\langle \mathbf{k}'l'|e^{i\mathbf{q}\cdot\mathbf{r}}|\mathbf{k}l\rangle|^2, \tag{6}$$

where $|\mathbf{k}l\rangle$ and $E_{\mathbf{k}l}$ are the eigenstates and eigenvalues of the TB Hamiltonian Eq. (1), respectively, with l being the band index, $\mathbf{k}'=\mathbf{k}+\mathbf{q}$, $\delta \to 0^+$, the integral is taken over the whole Brillouin zone (BZ), and the sum is calculated over all bands in the TB Hamiltonian Eq. (1). Note that, when the rotation angle goes down to 3.14°, the unit cell contains 1986 orbitals. The calculation of the polarization function from the Lindhard function becomes a numerical task due to the huge toll of diagonalization. On the contrary, in the Kubo formula in Eq. (5), the exact diagonalization of the Hamiltonian is unnecessary. So we can compute the dynamical polarization for systems with tiny rotation angles [37]. The accuracy of the Kubo formula will pave the way to further investigate collective excitations of TBG near the magic angle in a full TB model. Therefore, in the following, to check the validity of the Kubo formula, we will compare the polarization function obtained from the Kubo formula with the ones obtained from the Lindhard function.
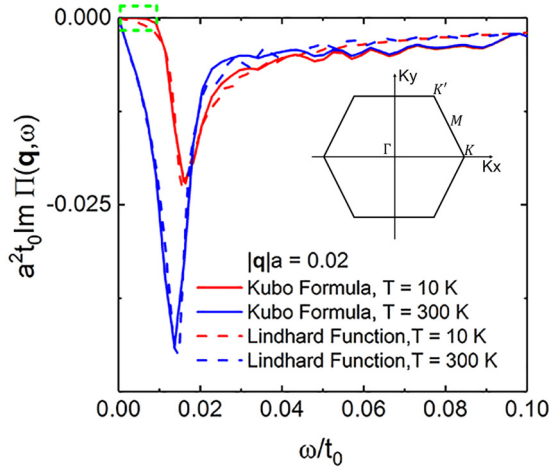
FIG. 1. The imaginary part of the polarization function of rigid TBG with $\theta = 6.01°$ computed from Kubo formula (solid line) and from Lindhard function (dashed line) for $T = 10$ K (red line) and $T = 300$ K (blue line). The inset is the Brillouin zone of TBG. The wave vector **q** along Γ-K is $|\mathbf{q}|a = 0.02$, $a = 2.46$ Å being the lattice constant, and the chemical potential is $\mu = 0$. The hopping parameters t_0 and t_1 are 2.78 eV and 0.33 eV, respectively.

With the polarization function acquired from either Kubo formula Eq. (5) or Lindhard function Eq. (6), the dielectric function that describes the electronic response to extrinsic electric perturbation can be written within the random phase approximation as

$$\varepsilon(\mathbf{q}, \omega) = 1 - V(q)\Pi(\mathbf{q}, \omega), \qquad (7)$$

in which $V(q) = 2\pi e^2/(\varepsilon_B q)$ is the Fourier component of the two-dimensional Coulomb interaction, with ε_B being the background dielectric constant. $\varepsilon_B = 1$ and $\varepsilon_B = 3.03$ represent the dielectric constant of the air and hexagonal boron nitride (hBN), respectively, in our calculations. The energy loss function can be expressed as

$$S(\mathbf{q}, \omega) = -\text{Im}(1/\varepsilon(\mathbf{q}, \omega)). \qquad (8)$$

To test the accuracy of the Kubo formula, we compare the polarization functions with that obtained from the Lindhard function at various angles and temperatures T. For twisted bilayer graphene with a large rotation angle, for instance, $\theta = 21.78°$, polarization functions obtained from the Lindhard function and the Kubo formula show remarkably quantitative agreement (not shown here). Furthermore, for smaller angles, the validity of the Kubo formula is tested in a smaller **q** that is located in the first Brillouin zone, see the inset in Fig. 1. The results from the Kubo formula are still in good agreement with the ones from the Lindhard function. Moreover, the temperature has an obvious impact on the polarization function, especially, for the imaginary part in the low-energy range which corresponds to the emergence of excitations at chemical potential $\mu = 0$ eV. As we can see from the green dashed rectangle in Fig. 1, excitations are induced from $\omega/t_0 = 0$ at 300 K, whereas they are forbidden in the energy range from $\omega/t_0 = 0$ to $\omega/t_0 = 0.01$ at 10 K. The difference could be explained as a result of the modification of the electronic distribution near the electric neutrality point at different tem-
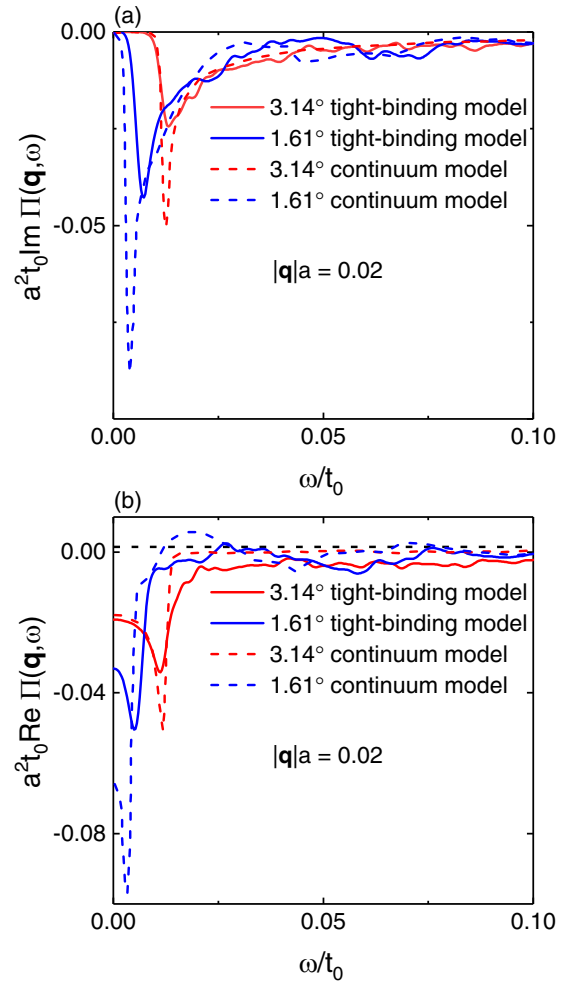

FIG. 2. Comparison of the polarization function computed by using the full tight-binding model (solid lines) and the effective continuum model (dashed lines) at $T = 1$ K and $\mu = 0$. (a) The imaginary part and (b) real part of polarizations for rigid TBG with rotation angles 3.14° (red lines) and 1.61° (blue lines). The wave vector **q** along Γ-K is $|\mathbf{q}|a = 0.02$, $a = 2.46$ Å being the lattice constant. The hopping parameters t_0 and t_1 are 2.78 eV and 0.33 eV, respectively. The black dashed line indicates the zero of the real part of dielectric function with the background dielectric constant $\epsilon_B = 1$. The data of the polarization from the continuum model are extracted from Ref. [12].

peratures. These remind us that temperature can be a crucial factor to tune the collective excitations in TBG.

The continuum model, as an effective low-energy model, has been broadly utilized to explore collective excitations in TBG [12,38,40]. In this part, the polarization functions from a full TB model are compared to the ones obtained from the continuum model in Ref. [12]. In the TB model, the Kubo formula is used to obtain the polarizations for TBG with rotation angle $\theta = 1.61°$ and $\theta = 3.14°$. The results in Fig. 2(b) show that, as a whole, the polarization functions from the TB resemble ones from the continuum model at a low energy window, except for the minor difference of the positions and magnitudes of the dips. As for the collective excitations, it is not possible to observe a plasmon mode at a relative large
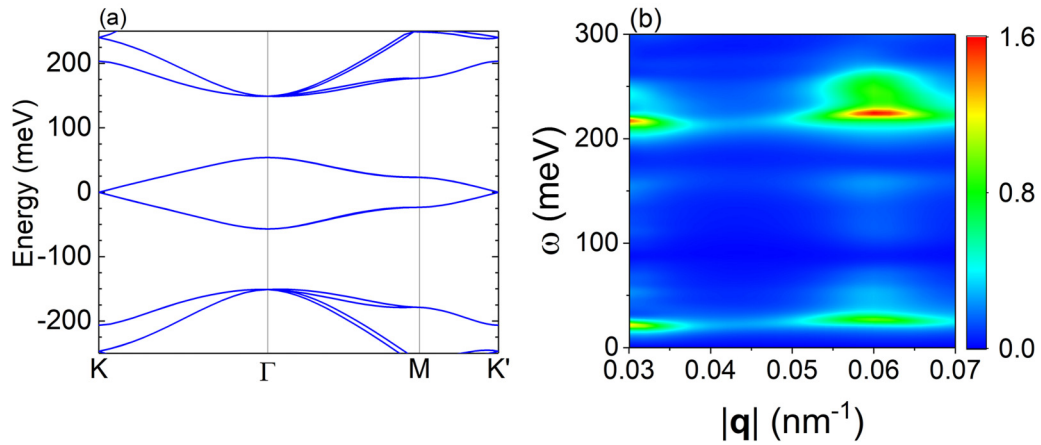
FIG. 3. Reproduce the experimentally collective excitation for twisted bilayer graphene with twist angle 1.35°. (a) The band structure obtained from a tight-binding calculation. Similar to the result in Ref. [11], a band gap with the value of 100 meV is obtained by assuming that interlayer hoppings of A sublattices and B sublattices are reduced to zero with hopping parameters $t_0 = 3.2$ eV and $t_1 = 0.49$ eV. (b) The loss function $S = -\text{Im}(1/\varepsilon)$ as functions of ω and $|\mathbf{q}|$ with $\mu = 0$ and $T = 300$ K. The plasmon mode above 200 meV is the one observed in the experiment [11].

rotation angle 3.14° without doping. It is verified from the real part of polarization functions in both models where the curves fail to cross the dashed black line in Fig. 2(b). For TBG with $\theta = 1.61°$, when the dielectric function in Eq. (7) in the main text satisfies $\text{Re}\epsilon(\mathbf{q}, \omega) = 0$, possible plasmon modes appear in both continuum models and TB model calculations. All in all, the accuracy of the Kubo formula is verified by comparing the results with these obtained from the Lindhard function shown in the main text of the Methods section and by the excellent agreement of polarizations in the full TB model and continuum model. Therefore, the Kubo formula in a full TB model can be further used to explore the collective properties of TBG near the magic angle.

III. PLASMONIC PROPERTIES OF TBG NEAR MAGIC ANGLE

A. Reproduce the experimentally collective plasmon

In a recent experiment, an interband plasmon mode with a value around 200 meV was reported in the charge-neutral TBG near the magic angle [11]. The band structure of such a system had a large band gap of 100 meV at the Γ point between the flat band and the first excited band in the conduction or valence bands. Such an unusual band gap could be explained by the extremely suppressed intrasublattice interlayer interaction due to the electron-electron interaction or extrinsic effects, for instance, the way samples are fabricated and the hBN encapsulation [11]. In fact, in our investigation of the magic angle in Appendix, the maximum band gap appears in the magic angle samples and has a value around 40 meV. In Ref. [11], the suppression of AA interlayer interactions can be realized by reducing the interlayer coupling in the AA regions u_0 in a continuum model. Here, we reproduce the large band gap by locally tuning the AA interlayer hopping in the full TB model. In the superlattice cell with twist angle $\theta = 1.35°$, all the atoms can be separated into two sublattices: Sublattice A and sublattice B. By changing the interlayer hopping parameter of intrasublattice A (intrasublattice B) to 0 (such approximation resembles the transformation of effective

AA and BB interlayer coupling u_0 to zero in the continuum model [31,40]), we obtain a band gap of 100 meV as shown in Fig. 3(a). The band structure shows great agreement with the one obtained from the continuum model in Ref. [11]. The corresponding energy loss function Eq. (8) can be obtained by using the Kubo formula Eqs. (5) and (7) in our full TB model. As shown in Fig. 3(b), the loss functions are calculated within wave vectors $|\mathbf{q}|$ that are accessible and detected in the experiment [11]. The plasmon mode takes place with energy near 210 meV, showing good agreement with the experimental plasmon distribution in Ref. [11] and theoretical results obtained from the continuum model with $u_0 = 0$ in Ref. [40]. Note that in the result shown in Fig. 3, the lattice relaxations are taken into account in the calculation (see details in Appendix A). The extreme consistency with the experimental results verifies the accuracy and promising applications of our method.

B. Plasmon spectrum near magic angle

Next, we utilize the Kubo formula in a full TB model to theoretically explore collective excitations in TBG near the magic angle. Two samples with different rotation angles are created, one is with $\theta = 1.35°$ and the other is the experimentally detected magic angle $\theta = 1.05°$. We explicitly discuss how to achieve the experimental magic angle $\theta = 1.05°$ with our full TB model in Appendix. The atomic relaxations are taken into account in the calculations. Plasmon modes discovered from these excitations can be detected by experimental technologies, such as S-SNOM, electron energy loss spectroscopy, and near-field experiments. In experiments, when plasmon modes with frequency ω_p exist with low damping, the electron energy loss spectra possess sharp peaks at $\omega = \omega_p$. Here, the energy loss function $-\text{Im}(1/\epsilon(\mathbf{q}, \omega))$ is calculated with the dielectric function obtained from Eq. (7) and the polarization function obtained from the Kubo formula in Eq. (5). Plasmon spectrums of the TBG with two different rotation angles 1.35° and 1.05° are illustrated in Fig. 4. The
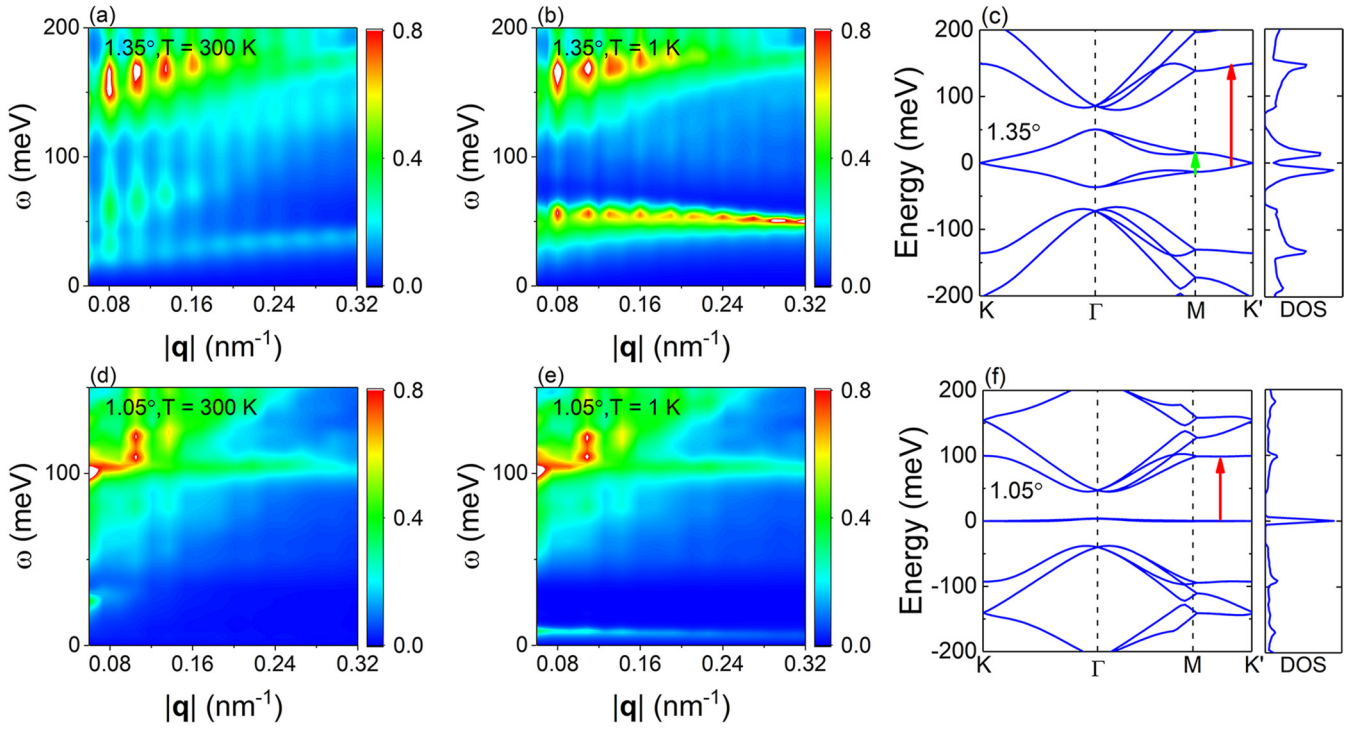
FIG. 4. The loss function $-\mathrm{Im}(1/\varepsilon)$ change with the frequency ω and wave vector $\mathbf{q}$ for relaxed TBG with twist angles 1.35° and 1.05° at temperatures (a), (d) $T = 300$ K and (b), (e) $T = 1$ K, respectively. The possible interband transitions are indicated by red and green arrows in the band structure for (c) $\theta = 1.35°$ and (f) $\theta = 1.05°$. The wave vector is along the Γ-K direction. The chemical potential is $\mu = 0$ and the background dielectric constant $\epsilon_B = 3.03$ corresponds to the hexagonal boron nitride (hBN) substrate. The hopping parameters $t_0 = 2.8$ eV and $t_1 = 0.44$ eV are utilized in the calculation and all the hopping terms follow the SK relations.

corresponding band structures of the two angles are also plotted in Figs. 4(c) and 4(f), respectively.

For TBG with $\theta = 1.35°$, interband plasmon modes close to 150 meV appear at both $T = 300$ K and 1 K, which are attributed to the interband transitions from the valence band near the Fermi energy to the conduction band located at 150 meV [red arrow in Fig. 4(c)]. These modes are similar to the ones around 200 meV in Fig. 3 that originate from the collective oscillations of electrons in the AA region of TBG [11]. The 150 meV plasmon modes disperse within particle-hole continuum in Figs. 5(a) and 5(b) with fast damping into electron-hole pairs. Other interband plasmon modes have the energy of 50 meV at temperature 1 K in Fig. 4(b), which can be interpreted as collective transitions between near zero-energy four bands [green arrow in Fig. 4(c)], and resemble the ones obtained by the continuum model in undoped and unrelaxed 1.30° TBG [12]. As we can see from Fig. 5(b), the $-\mathrm{Im}\Pi(\mathbf{q}, \omega)$ is zero around 50 meV energy, showing that the 50 meV plasmons avoid Laudau damping from the interaction of collective excitations and single particle-hole transitions. At room temperature, the long-lived 50 meV plasmon modes split into two. One kind of mode has energy around 25 meV and the other above 50 meV. Both of them are damping plasmons with the increased wave vectors. Nevertheless, compared to the remarkable variations of the plasmonic properties with temperature, the main feature of the low energy plasmons is still conserved from $T = 0$ to $T = 300$ K in the continuum model [12]. As shown in Fig 5(a), in contrast to the scenario at 1 K temperature, new single-particle transitions

simultaneously occur around the plasmonic energy. Obviously, at nonzero temperature, some states fluctuate around
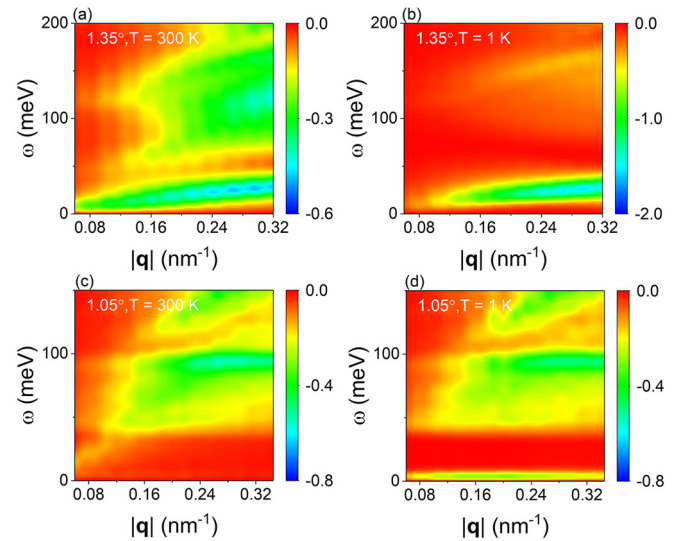

FIG. 5. $-\mathrm{Im}\Pi(\mathbf{q}, \omega)$ change with the frequency ω and wave vector $\mathbf{q}$ for relaxed TBG with 1.35° and 1.05° at (a), (c) $T = 300$ K and (b), (d) $T = 1$ K, respectively. The wave vector is along the Γ-K direction. The chemical potential is $\mu = 0$ and the background dielectric constant $\epsilon_B = 3.03$ corresponds to the hBN substrate. The hopping parameters are $t_0 = 2.8$ eV and $t_1 = 0.44$ eV and all the hopping terms follow the SK relations.

the Fermi energy, leading to the conduction band partially filled near the Fermi energy. Therefore, different from the result at 1 K, extra single-particle intraband transitions are induced at room temperature, giving rise to remarkable variations of the particle-hole continuum spectrum in Figs. 5(a) and 5(b).

For TBG with $\theta = 1.05°$, the first obvious plasmon modes in Fig. 4 locate at 100 meV at both $T = 300$ K and 1 K. These plasmons are also coming from the interband transitions illustrated in Fig. 4(f) (red arrow). The energy of the plasmons is smaller than the one discovered in TBG with $\theta = 1.35°$ since the van Hove singularity is located at the energy around 100 meV. These modes are damping ones as they cross the nonzero region in the particle-hole continuum spectrum in Figs. 5(c) and 5(d), and it becomes clear with a fine and flat shape with momentum larger than 0.2 nm^{-1}. At room temperature, different from the two splitting plasmons in TBG with 1.35°, the plasmons that stem from the collective transitions among four flat bands vanish for TBG with 1.05° in Fig. 4(d). Besides, single-particle excitations are almost not allowed in flat bands below 40 meV in Fig. 5(c), corresponding to the experimental value of band gap between the flat bands and the excited bands at the Γ point in Fig. 4(f). When the temperature declines to the critical temperature 1 K at which the superconductivity can be detected in the magic-angle system [2,3], a thin plasmon mode with energy of 9 meV emerges and stretches to large q in Fig. 4(e), which is contributed to the collective excitations among flat bands (flat-band plasmon). Interestingly, unlike the low energy interband plasmons in the 1.35° sample, this plasmonic mode is contributed by both interband and intraband transitions even when the chemical potential is zero. If we check the four flat bands of the 1.05° sample in Fig. 9(b), the two valence bands are distorted upward above zero energy at the Γ point, thus giving rise to extra intraband transitions. Meanwhile, underneath the collective flat-band plasmon mode, the particle-hole transitions arise with occupying a tiny energy region ranging from 0 to 8 meV in Fig. 5(d). As a result, this plasmon mode extends above the edge of this tiny energy zone and is free from the Laudau damping.

The common feature of the plasmon modes in both cases is that they are ultraflat over the whole **q** vectors, which is in good agreement with the findings calculated by using the continuum model [12]. However, the flat plasmon modes are not explicitly predicted in some works, in which the plasmons are derived from local optical conductivity [38,40]. These collective interband transitions denoted by arrows in Figs. 4(c) and 4(f) are related to the electronic excitations in AA stacking regions of supercells in small angle TBG, as electrons of the four flat bands near zero energy are localized in such region. The higher energy plasmon mode can be changed at two different angles due to the variation of the Van Hove singularity with the twist angle, but rarely affected at different temperature. On the contrary, temperature gives rise to obvious transformation of the lower energy mode in both angles. Furthermore, the low-energy updamped plasmon mode emerging at the magic angle can extend from Γ to K point of the boundary of the first Brillouin zone, in continuum model [13], yet this mode gradually turns weak when q approaches the K point (0.32/nm) in Fig. 4(e).

Furthermore, it deserves checking if this flat-band plasmon is determined by the flatness of the four flat bands. As seen from the loss function in Fig. 6(a), for TBG with three different rotation angles where flat bands appear as shown in Fig. 9, the position of the first peak, corresponding to the energy of the flat-band plasmon E_p, reaches the minimum energy for TBG with the magic angle 1.05°. The first peak of the loss functions for TBG with the other two angles 1.08° and 1.02° have the same higher energy since their bandwidths of flat bands are almost identical but both larger than that of the magic angle. What enlightens us here is that the different electronic responses to various bandwidths could support us unveiling the flatness of flat bands in a large moiré system where the calculations of the band structure becomes prohibitively expensive.

In the previous parts, effects of the temperature on plasmons have been studied briefly in undoped TBG. How the flat-band plasmons of TBG with 1.05° change with the temperatures over a large range from 1 K to 300 K pushes us to explore the loss functions under several temperatures, which is plotted in Fig. 6(b). The temperature suppresses significantly collective excitations between flat bands since the magnitude of the first peak declines sharply with increased temperatures. In Ref. [13], doped magic-angle TBG also has an undamped plasmon mode with energy around 7 meV, which is similar to aforementioned flat-band plasmons in our undoped case. Both of them are contributed from intraband and interband transitions. But how the doping level varies the flat-band plasmon is unclear. Here, we further investigate the influence of the chemical potential on flat-band plasmons in TBG with magic angle in Fig. 6(c). When the flat band is doped to a relatively low level of 2 meV and is partially filled, the first peak of loss function is overlapped with the undoped one. The flat-band plasmon is not affected by the low-level doping. For a higher doping level, for instance, 6 meV, that reaches the edge of flat bands, there is a weak electronic response with the first peak fading away. The filled flat bands at doping level 10 meV forbid all collective excitations from these flat bands. In addition, doping TBG to 6 meV has an equivalent effect to increasing temperature to 300 K in terms of the first peak of loss function. Therefore, it is essential to keep a low doping level and low temperature if one wishes to observe the flat-band plasmon mode in TBG with the magic angle.

IV. SUMMARY AND DISCUSSION

In summary, collective excitations in TBG are explicitly investigated by utilizing the Kubo formula in the frame of a full TB model. We mainly compare plasmonic properties for TBG with angles 1.35° and 1.05° at different temperatures. For the higher energy plasmon modes, they are conserved at both 300 K and 1 K and interact with single-particle electron-hole transitions, giving rise to a quick damping rate. Interestingly, undamped plasmon modes in the low energy range can be well defined since they go through the zero regions of the particle-hole spectrum. Increasing temperature from 1 K to 300 K turns the single undamped plasmon mode with lower energy into two damped bands in 1.35° sample. At magic angle 1.05°, the undamped flat-band plasmon mode disappears at 300 K but emerges at 1 K with the minimum energy due to
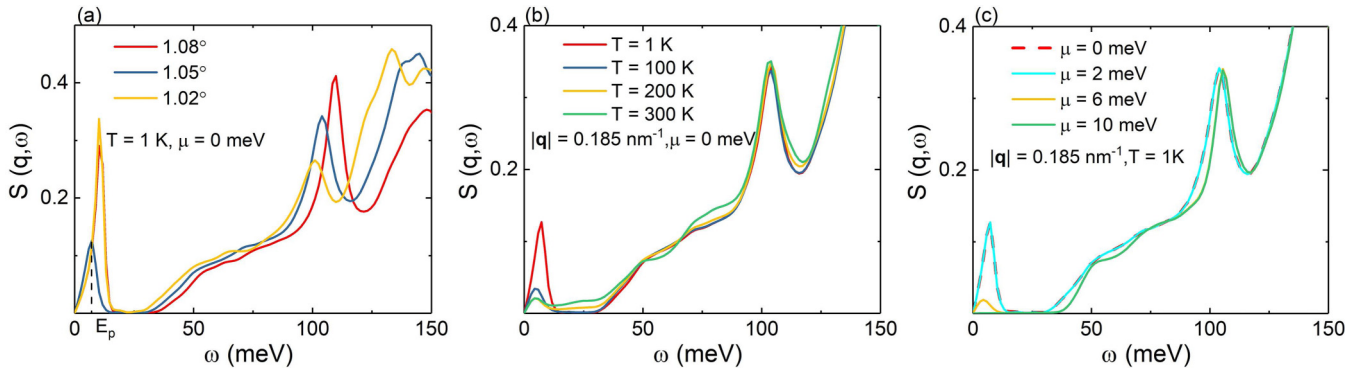
FIG. 6. Loss function $S(\mathbf{q}, \omega) = -\text{Im}(1/\epsilon(\mathbf{q}, \omega))$ of twisted bilayer graphene (a) near 1.05° at T = 1 K, (b) with $\theta = 1.05°$ at various temperatures and (c) with magic angle 1.05° for different chemical potentials μ. The hopping parameters are the same as that in Fig. 5.

the narrowest bandwidth of flat bands. The angle dependence of flat-band plasmons near 1.05° reflects different bandwidths of flat bands. The comparison of doping and temperature effects on the flat-band plasmonic peaks in loss function could guide us to study the flatness of flat bands in experiments. Lastly, in our simulation, the correct polarization functions are calculated with $\mathbf{q}$ inside the Brillouin zone, whereas the local field effect is supposed to be included when $\mathbf{q}$ approaches the zone boundary [52,53]. The local field effects are discussed in TBG with small twist angles and can be ignored safely [12] but are still worth being explored in even larger systems at the series of different magic angles. The many-body effect on the flat-band plasmons can be also explored via our method and self-consistent Hartree approach in full TB model [54].

Recently, it has been theoretically predicted that unconventional superconductivity in TBG is mediated by the purely collective electronic modes [18,19]. Therefore, a deep understanding of collective excitations in TBG may also shed light on the plasmonic superconductivity. Last but not least, the quantum Doppler effect was theoretically predicted in the flat-band plasmon [55]. Such significant plasmonic nonreciprocity $\omega_p(\mathbf{q}) \neq \omega_p(-\mathbf{q})$ proves that TBG with the magic angle is a promising optoelectronics platform. For instance, it can be utilized to develop optoelectronic devices with suppressed backscattering [56,57]. More fundamental and practical applications refer to Ref. [55].

APPENDIX: TUNE THE MAGIC ANGLE

Effects of lattice relaxation on electronic properties of TBG near the magic angle have been theoretically investigated by utilizing both the TB model and the continuum model [23,24,31,34]. For instance, in a full TB model with the hopping parameters $t_0 = 2.7$ eV and $t_1 = 0.48$ eV, the in-plane relaxation tunes the magic angle from 1.20° to around 1.12° [23]. In this Appendix, we consider a full relaxation (both out-of-plane and in-plane) effect on the band structure of TBG around the magic angle, from which plasmons in Sec. III are investigated in such a relaxed atomic structure. Atomic relaxation of TBG is performed via classical simulation package LAMMPS [58]. The intralayer and interlayer interactions are simulated with long-rang carbon bond-order potential [59] and Kolmogorov-Crespi potential [60], respectively, which are implemented to show similar experimental lattice [25]. We assume the relaxed samples keep the period of the rigidly TBG. Effects of relaxation on bands of TBG
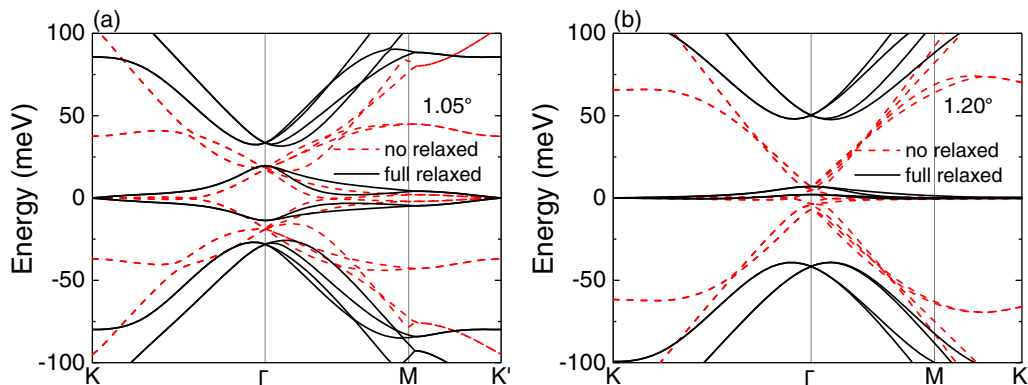

FIG. 7. Band structure of full relaxed (black solid lines) and unrelaxed (red dashed lines) twisted bilayer graphene with twist angles (a) $\theta = 1.05°$ and (b) $\theta = 1.20°$. The hopping parameters t_0 and t_1 are 2.7 eV and 0.48 eV, respectively.
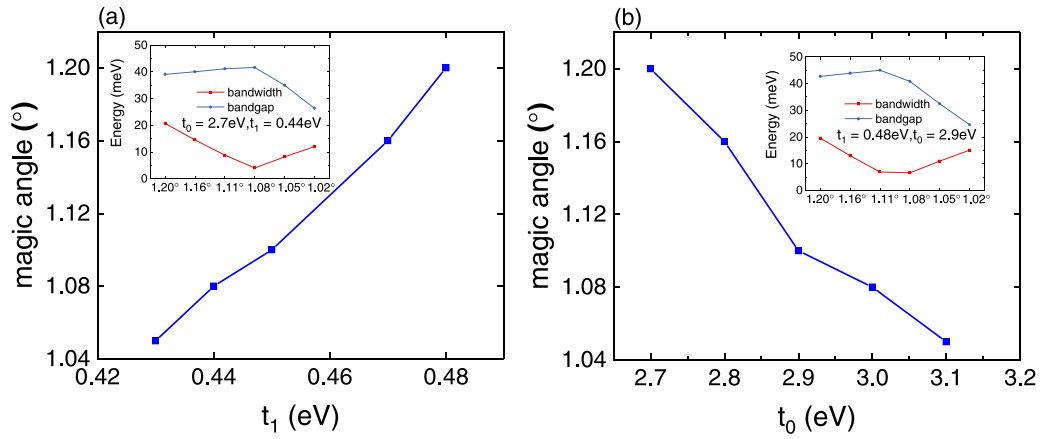
FIG. 8. Evolution of magic angle with different intralayer hopping or interlayer hopping parameters in the relaxed TBG. (a) The variation of magic angle with different interlayer hopping parameters t_1 and fixed $t_0 = 2.7$ eV. The inset indicates the variation of bandwidth and band gap near the magic angle $1.08°$ with a couple of hopping parameters $t_0 = 2.7$ eV and $t_1 = 0.44$ eV. (b) The value of magic angle changes with different intralayer hopping parameter t_0 and fixed $t_1 = 0.48$ eV. The inset shows the change of bandwidth and band gap with various rotation angles and fixed hopping parameters $t_1 = 0.48$ eV and $t_0 = 2.9$ eV.

with rotation angles $1.05°$ and $1.20°$ are displayed in Fig. 7. The interaction parameters are $t_0 = 2.7$ eV and $t_1 = 0.48$ eV, which are usually used in literature [22,23]. Apparently, the relaxation separates four bands near the neutral point from other excited valence and conduction bands. The opened band gap at the Γ point (electron side) in the $1.05°$ system is about 14 meV and the bandwidth (the difference between Γ and K points in the conduction band) is measured to be 20 meV. The magic angle is still at $1.20°$, which has a maximum band gap of 43 meV and minimum bandwidth of 7 meV.

As expected from the experiment, in principle, the so-called magic angle $1.05°$ possesses the maximum band gap and the minimum bandwidth in Fig. 7. In this Appendix, we try to reproduce the experimentally magic angle $1.05°$ in our TB model. The works that the magic angle can be tuned by applying a pressure [3,61,62] enlighten us to shift the magic angle via changing the interlayer and intralayer hopping parameters. In this way, the magic angle can be also tuned in kagome twisted bilayer by altering t_1/t_0 [63]. As shown in Fig. 8, the magic angle can be shifted from a relatively large angle to a smaller one via gradually decreasing
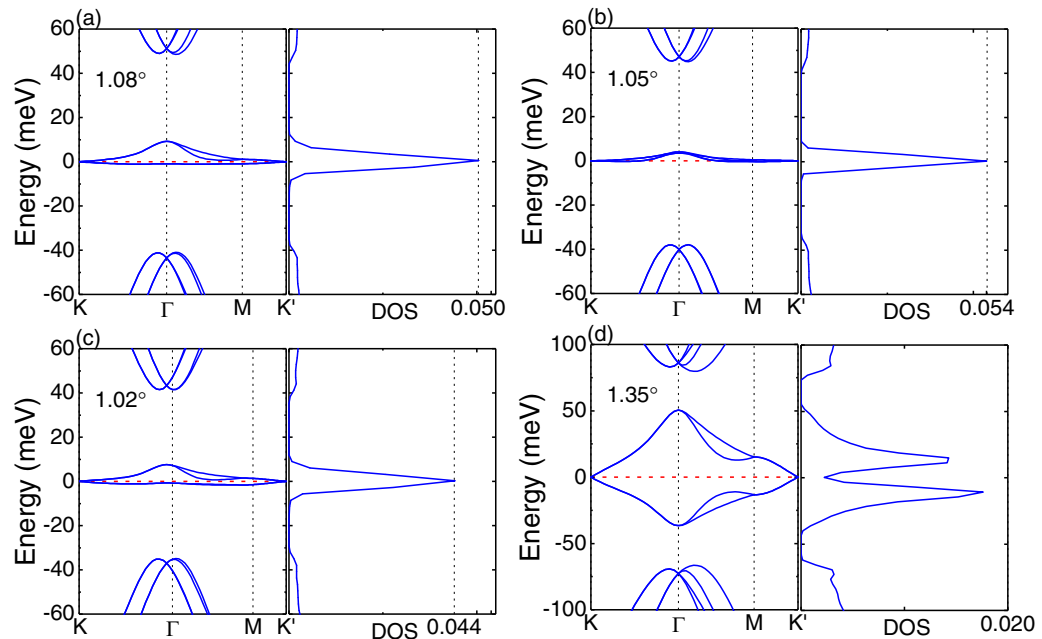

FIG. 9. Band structure and related density of states for relaxed TBG with twist angles (a) $1.08°$, (b) $1.05°$, (c) $1.02°$, and (d) $1.35°$. The vertical dashed lines of DOS in (a)–(c) denote the maximum value of DOS at zero Fermi energy. The red dashed lines denote the zero Fermi energy. The hopping parameters t_0 and t_1 are 2.8 eV and 0.44 eV, respectively.

the interlayer hopping t_1 or enhancing the intralayer hopping t_0. For instance, at two given sets of t_0 and t_1 in insets of Figs. 8(a) and 8(b), which have the magic angle at $1.08°$ and $1.1°$, respectively, the bandwidth and band gap vary with the twist angle and reach the extremum at the magic angle. The two features are also identified as the definition of magic angle.

We tune the intralayer and interlayer interaction in our theoretical model to shift the four extremely flat bands from $1.20°$ to $1.05°$, close to which superconductivity is observed in experiments [2]. Such a method is similar to the modulation of the effective interlayer coupling and Fermi velocity in the continuum model [62]. It shows that the flat band can be shifted from $1.20°$ to $1.05°$ by enhancing the intralayer inter-action, t_0 from 2.7 eV to 2.8 eV and weakening the interlayer interaction, t_1 from 0.48 eV to 0.44 eV. For TBG with different values of magic angles, the bandwidths and band gaps are different, which results in varied energy positions of the flat-band plasmon. The band structures and electronic DOS for TBG near $1.05°$ are plotted in Fig. 9, where the flattest band and the largest magnitude of DOS peak located at the Dirac point are at the angle $\theta = 1.05°$. The sharp peak of DOS is conserved at angles $1.08°$ and $1.02°$, which are very close to the magic angle $\theta = 1.05°$. The bandwidth smaller than 10 meV also appears in these two angles. Therefore, the conception of the single magic angle can be broaden toward magic angles [34]. Besides, the electronic-side band gap 42 meV and bandwidth 9 meV of flat bands in TBG with $\theta = 1.08°$ are consistent with experimental values. Apart from these three magic angles with flat bands and corresponding Dirac peak in DOS at the neutral point, the band structure and DOS of the TBG with $1.35°$ are also obtained, showing the absence of a Dirac peak at the neutral point and of the flat band. In our TB result, the band gap is underestimated compared to the one in experiments [11] if only relaxation effects are taken into account. A parameterized TB model with relaxed atomic structures, which is able to reproduce key features of band structure near the magic angle, can be used to further explore collective behaviors of electrons in the main text, such as plasmons near the magic angle.

[1] R. Bistritzer and A. H. MacDonald, Proc. Natl. Acad. Sci. USA **108**, 12233 (2011).

[2] Y. Cao, V. Fatemi, S. Fang, K. Watanabe, T. Taniguchi, E. Kaxiras, and P. Jarillo-Herrero, Nature (London) **556**, 43 (2018).

[3] M. Yankowitz, S. Chen, H. Polshyn, Y. Zhang, K. Watanabe, T. Taniguchi, D. Graf, A. F. Young, and C. R. Dean, Science **363**, 1059 (2019).

[4] Y. Cao, V. Fatemi, A. Demir, S. Fang, S. L. Tomarken, J. Y. Luo, J. D. Sanchez-Yamagishi, K. Watanabe, T. Taniguchi, E. Kaxiras et al., Nature (London) **556**, 80 (2018).

[5] A. Kerelsky, L. J. McGilly, D. M. Kennes, L. Xian, M. Yankowitz, S. Chen, K. Watanabe, T. Taniguchi, J. Hone, C. Dean et al., Nature (London) **572**, 95 (2019).

[6] Y. Choi, J. Kemmer, Y. Peng, A. Thomson, H. Arora, R. Polski, Y. Zhang, H. Ren, J. Alicea, G. Refael et al., Nat. Phys. **15**, 1174 (2019).

[7] X. Lu, P. Stepanov, W. Yang, M. Xie, M. A. Aamir, I. Das, C. Urgell, K. Watanabe, T. Taniguchi, G. Zhang et al., Nature (London) **574**, 653 (2019).

[8] Y. Xie, B. Lian, B. Jäck, X. Liu, C.-L. Chiu, K. Watanabe, T. Taniguchi, B. A. Bernevig, and A. Yazdani, Nature (London) **572**, 101 (2019).

[9] Y. Jiang, X. Lai, K. Watanabe, T. Taniguchi, K. Haule, J. Mao, and E. Y. Andrei, Nature (London) **573**, 91 (2019).

[10] M. Serlin, C. Tschirhart, H. Polshyn, Y. Zhang, J. Zhu, K. Watanabe, T. Taniguchi, L. Balents, and A. Young, Science **367**, 900 (2020).

[11] N. C. Hesp, I. Torre, D. Rodan-Legrain, P. Novelli, Y. Cao, S. Carr, S. Fang, P. Stepanov, D. Barcons-Ruiz, H. Herzig-Sheinfux et al., arXiv:1910.07893.

[12] T. Stauber and H. Kohler, Nano Lett. **16**, 6844 (2016).

[13] C. Lewandowski and L. Levitov, Proc. Natl. Acad. Sci. USA **116**, 20869 (2019).

[14] T. Stauber, T. Low, and G. Gómez-Santos, Nano Lett. **20**, 8711 (2020).

[15] L. Brey, T. Stauber, T. Slipchenko, and L. Martín-Moreno, Phys. Rev. Lett. **125**, 256804 (2020).

[16] X. Lin, Z. Liu, T. Stauber, G. Gómez-Santos, F. Gao, H. Chen, B. Zhang, and T. Low, Phys. Rev. Lett. **125**, 077401 (2020).

[17] A. V. Rozhkov, A. Sboychakov, A. Rakhmanov, and F. Nori, Phys. Rep. **648**, 1 (2016).

[18] G. Sharma, M. Trushin, O. P. Sushkov, G. Vignale, and S. Adam, Phys. Rev. Res. **2**, 022040(R) (2020).

[19] C. Lewandowski, D. Chowdhury, and J. Ruhman, arXiv:2007.15002.

[20] J. González and T. Stauber, Phys. Rev. Lett. **124**, 186801 (2020).

[21] E. S. Morell, J. Correa, P. Vargas, M. Pacheco, and Z. Barticevic, Phys. Rev. B **82**, 121407(R) (2010).

[22] G. Trambly de Laissardière, D. Mayou, and L. Magaud, Phys. Rev. B **86**, 125413 (2012).

[23] N. N. T. Nam and M. Koshino, Phys. Rev. B **96**, 075311 (2017).

[24] M. Angeli, D. Mandelli, A. Valli, A. Amaricci, M. Capone, E. Tosatti, and M. Fabrizio, Phys. Rev. B **98**, 235137 (2018).

[25] F. Guinea and N. R. Walet, Phys. Rev. B **99**, 205134 (2019).

[26] N. Leconte, S. Javvaji, J. An, and J. Jung, arXiv:1910.12805.

[27] J. M. B. Lopes dos Santos, N. M. R. Peres, and A. H. Castro Neto, Phys. Rev. Lett. **99**, 256802 (2007).

[28] J. L. Dos Santos, N. Peres, and A. C. Neto, Phys. Rev. B **86**, 155449 (2012).

[29] P. Moon and M. Koshino, Phys. Rev. B **87**, 205404 (2013).

[30] S. Fang and E. Kaxiras, Phys. Rev. B **93**, 235153 (2016).

[31] M. Koshino, N. F. Q. Yuan, T. Koretsune, M. Ochi, K. Kuroki, and L. Fu, Phys. Rev. X **8**, 031087 (2018).

[32] P. Lucignano, D. Alfè, V. Cataudella, D. Ninno, and G. Cantele, Phys. Rev. B **99**, 195419 (2019).

[33] G. Tarnopolsky, A. J. Kruchkov, and A. Vishwanath, Phys. Rev. Lett. **122**, 106405 (2019).

[34] S. Carr, S. Fang, Z. Zhu, and E. Kaxiras, Phys. Rev. Res. **1**, 013001 (2019).

[35] W. Yan, W.-Y. He, Z.-D. Chu, M. Liu, L. Meng, R.-F. Dou, Y. Zhang, Z. Liu, J.-C. Nie, and L. He, Nat. Commun. **4**, 2159 (2013).

[36] L. Huder, A. Artaud, T. Le Quang, G. T. de Laissardiere, A. G. M. Jansen, G. Lapertot, C. Chapelier, and V. T. Renard, Phys. Rev. Lett. **120**, 156405 (2018).

[37] H. Shi, Z. Zhan, Z. Qi, K. Huang, E. van Veen, J. Á. Silva-Guillén, R. Zhang, P. Li, K. Xie, H. Ji *et al.*, Nat. Commun. **11**, 371 (2020).

[38] T. Stauber, P. San-Jose, and L. Brey, New J. Phys. **15**, 113050 (2013).

[39] Y. Cao, J. Y. Luo, V. Fatemi, S. Fang, J. D. Sanchez-Yamagishi, K. Watanabe, T. Taniguchi, E. Kaxiras, and P. Jarillo-Herrero, Phys. Rev. Lett. **117**, 116804 (2016).

[40] P. Novelli, I. Torre, F. H. L. Koppens, F. Taddei, and M. Polini, Phys. Rev. B **102**, 125403 (2020).

[41] S. Yuan, H. De Raedt, and M. I. Katsnelson, Phys. Rev. B **82**, 115448 (2010).

[42] G. J. Slotman, M. M. van Wijk, P.-L. Zhao, A. Fasolino, M. I. Katsnelson, and S. Yuan, Phys. Rev. Lett. **115**, 186801 (2015).

[43] S. Yuan, R. Roldán, M. Katsnelson, and F. Guinea, Phys. Rev. B **90**, 041402(R) (2014).

[44] S. Yuan, R. Roldan, and M. I. Katsnelson, Solid State Commun. **152**, 1446 (2012).

[45] H. A. Le and V. N. Do, Phys. Rev. B **97**, 125136 (2018).

[46] J. C. Slater and G. F. Koster, Phys. Rev. **94**, 1498 (1954).

[47] G. Yu, Z. Wu, Z. Zhan, M. I. Katsnelson, and S. Yuan, npj Comput. Mater. **5**, 122 (2019).

[48] A. Hams and H. De Raedt, Phys. Rev. E **62**, 4365 (2000).

[49] R. Kubo, J. Phys. Soc. Jpn. **12**, 570 (1957).

[50] S. Yuan, R. Roldán, and M. I. Katsnelson, Phys. Rev. B **84**, 035439 (2011).

[51] G. Giuliani and G. Vignale, *Quantum Theory of the Electron Liquid* (Cambridge University Press, Cambridge, 2005).

[52] S. L. Adler, Phys. Rev. **126**, 413 (1962).

[53] N. Wiser, Phys. Rev. **129**, 62 (1963).

[54] L. Rademaker, D. A. Abanin, and P. Mellado, Phys. Rev. B **100**, 205114 (2019).

[55] M. Papaj and C. Lewandowski, Phys. Rev. Lett. **125**, 066801 (2020).

[56] A. Kamal, J. Clarke, and M. Devoret, Nat. Phys. **7**, 311 (2011).

[57] S. Hua, J. Wen, X. Jiang, Q. Hua, L. Jiang, and M. Xiao, Nat. Commun. **7**, 13657 (2016).

[58] S. Plimpton, Fast parallel algorithms for short-range molecular dynamics, J. Comput. Phys. **117**, 1 (1995).

[59] J. H. Los, L. M. Ghiringhelli, E. J. Meijer, and A. Fasolino, Phys. Rev. B **72**, 214102 (2005).

[60] A. N. Kolmogorov and V. H. Crespi, Phys. Rev. B **71**, 235415 (2005).

[61] S. Carr, S. Fang, P. Jarillo-Herrero, and E. Kaxiras, Phys. Rev. B **98**, 085144 (2018).

[62] B. L. Chittari, N. Leconte, S. Javvaji, and J. Jung, Electron. Struct. **1**, 015001 (2018).

[63] F. Crasto de Lima, R. H. Miwa, and E. Suarez Morell, Phys. Rev. B **100**, 155421 (2019).